

Three-dimensional simulation of a new cooling strategy for proton exchange membrane fuel cell stack using a non-isothermal multiphase model



Guobin Zhang^{a,b}, Hao Yuan^b, Yun Wang^{b,*}, Kui Jiao^{a,*}

^a State Key Laboratory of Engines, Tianjin University, 135 Yaguan Road, Tianjin 300350, China

^b Renewable Energy Resources Laboratory, Department of Mechanical and Aerospace Engineering, University of California, Irvine, CA 92697-4075, USA

HIGHLIGHTS

- A new cooling strategy is investigated, which simplifies stack design.
- 3D multiphase simulation of a 5-cell stack with new cooling strategy was conducted.
- Two conditions were studied: finite vs. infinite convective heat transfer cooling.
- A maximum temperature variation of ~ 30 K is predicted in the stack.
- The new strategy needs to increase heat transfer coefficient for stack applications.

ARTICLE INFO

Keywords:

PEM fuel cell
Stack
3D
Multiphase
New cooling strategy

ABSTRACT

In this study, a new cooling strategy for a proton exchange membrane (PEM) fuel cell stack is investigated using a three-dimensional (3D) multiphase non-isothermal model. The new cooling strategy follows that of the Honda's Clarity design and further extends to a cooling unit every five cells in stacks. The stack consists of 5 fuel cells sharing the inlet and outlet manifolds for reactant gas flows. Each cell has 7-path serpentine flow fields with a counter-flow configuration arranged for hydrogen and air streams. The coolant flow fields are set at the two sides of the stack and are simplified as the convective heat transfer thermal boundary conditions. This study also compares two thermal boundary conditions, namely limited and infinite coolant flow rates, and their impacts on the distributions of oxygen, liquid water, current density and membrane hydration. The difference of local temperature between these two cooling conditions is as much as 6.9 K in the 5-cell stack, while it is only 1.7 K in a single cell. In addition, the increased vapor concentration at high temperature (and hence water saturation pressure) dilutes the oxygen content in the air flow, reducing local oxygen concentration. The higher temperature in the stack also causes low membrane hydration, and consequently poor cell performance and non-uniform current density distribution, as disclosed by the simulation. The work indicates the new cooling strategy can be optimized by increasing the heat transfer coefficient between the stack and coolant to mitigate local overheating and cell performance reduction.

1. Introduction

PEM (proton exchange membrane, also known as polymer electrolyte membrane) fuel cell, converting chemical energy stored in hydrogen into electricity, has been widely used in a variety of applications [1], including automobile (e.g. Mirai [2] and Clarity [3]), stationary [4] and distributed [5] power sources, portable application [6], back-up power [7], auxiliary power source for aerospace [8], etc. In particular, FCV (fuel cell vehicle) received considerable attention in the last few years. In 2017, Toyota started to sell its first commercial FCV named

“Mirai” [9]. Later Honda, Hyundai, GM and so on successively launched their own FCV models, and the fuel cell engines of Honda Clarity [10] and Hyundai NEXO [11] were selected as 2018 and 2019 Ward Ten Engines, respectively. By the middle of 2018, there were about 5000 FCVs in the world [12].

In the operation of PEM fuel cell, multiple transport phenomena occur, which are coupled with the electrochemical reactions. Proper water [13] and thermal management is of primary importance to PEM fuel cell operation for high efficiency and durability [14]. According to the thermodynamic theory, it is known that the reversible voltage of a

* Corresponding authors.

E-mail addresses: yunw@uci.edu (Y. Wang), kjiao@tju.edu.cn (K. Jiao).

Nomenclature			
C_p	heat capacity ($\text{J mol}^{-1} \text{K}^{-1}$)	κ_e	electric conductivity (S m^{-1})
D	diffusion coefficient ($\text{m}^2 \text{s}^{-1}$)	κ_{ion}	ionic conductivity (S m^{-1})
EW	equivalent weight of membrane	λ	membrane water content
E_{rev}	reversible voltage (V)	μ	dynamic viscosity ($\text{kg m}^{-1} \text{s}^{-1}$)
F	the Faraday's constant ($96,487 \text{ C mol}^{-1}$)	ρ	density (kg m^{-3})
h	convective heat transfer coefficient ($\text{W m}^{-2} \text{K}^{-1}$) or latent heat (J mol^{-1})	φ_e	electric potential (V)
I	current density (A m^{-2})	φ_{ion}	ionic potential (V)
J	volumetric reaction rate (A m^{-3})	<i>Subscripts and superscripts</i>	
J_{ion}	ionic current density (A m^{-2})	a	anode
K	intrinsic permeability (m^2)	c	cathode
k	relative permeability or thermal conductivity ($\text{W m}^{-1} \text{K}^{-1}$)	CL	catalyst layer
M	molar mass (kg mol^{-1})	d	membrane water
n_d	EOD coefficient	d-v	membrane water to vapor
P	pressure (Pa)	e	electrical
S	source term ($\text{kg m}^{-3} \text{s}^{-1}$, $\text{mol m}^{-3} \text{s}^{-1}$, A m^{-3} or W m^{-3})	eq	equivalent state
s	liquid saturation	eff	effective value
T	temperature (K)	g	gas phase
t	time (s)	H_2	hydrogen
u	velocity (m s^{-1})	H_2O	water
V_{out}	output voltage	i	gas species
Y_i	gas species mass fraction	ion	ionic
<i>Greek letters</i>		l	liquid phase
γ	water condensation/evaporation rate (s^{-1})	m	mass
δ	thickness (m)	mem	membrane
ε	porosity	mw	membrane water
η	overpotential (V)	O_2	oxygen
		T	temperature
		total	total
		u	momentum
		v-l	vapor to liquid phase

single PEM fuel cell is about 1.23 V [15]. In normal operation, the output voltage will reduce to about 0.6–0.7 V with a power density of 1.0 W cm^{-2} for state-of-the-art PEM fuel cell. In practical application, a number of fuel cells are connected one by one in a stack to meet practical power demand [16]. For example, the stack in FCV usually consists of 300–400 cells [17]. In the operation of a stack, fuel cells are interacted via the gas/liquid flows, temperature, and electric current, so the stack performance is the average over all the fuel cells, which may have different distributions of temperature, reactant gas, etc. [18]. This also makes the stack's water and thermal management much more difficult than a single cell.

So far, a few studies aiming to reveal stack operation in detail has been attempted. Devrim et al. [19] assembled an air-cooling 24-cell stack and measured individual cell voltages and open circuit voltages (OCVs), temperature profile and stack polarization curve. Amirfazli et al. [20] developed an experimentally validated analytical/numerical

model to investigate the influence of manifold geometry on temperature uniformity in a PEM fuel stack. In addition, they introduced a variable cross-sectional area manifold and concluded that the best manifold cross-sectional areas are different for U and Z configurations. Wen et al. [21] experimentally investigated the effects of the bolt configuration and clamping torque on performance of a 10-cell stack. They found that the maximum power density increases as the clamping torque and bolt number thanks to reduction of the contact resistance. Weng et al. [22] tested the performance of a fuel cell stack in both static and dynamic modes. In the static mode, the peak power densities for 1, 2 and 4-cell stack are 0.55, 0.47 and 0.39 W cm^{-2} , respectively, and cell performance decreases with increasing cell number in the stack. In the dynamic mode, they indicated that additional actions are required, e.g. purging water, to ensure high stack performance and maintain stability. In addition, manifolds [23] play an important role in stack operation providing that individual flow fields are connected at the

Table 1
Cooling methods for PEM fuel cells [12,39,40].

Cooling Method	Techniques/Materials	Advantages
Heat spreaders	Using highly thermal conductive material (e.g. copper) [41] or heat pipes [42] as heat spreaders	<ul style="list-style-type: none"> – Simple system – Small parasitic power – Very high thermal conductivity using heat pipes
Air cooling [45]	Separate air flow channels for cooling, suitable for 200 W–2 kW stacks [39,40]	<ul style="list-style-type: none"> – Simple system – Potential integration for fuel cell oxygen supply
Liquid cooling [46]	Cooling channels embedded in BPs using antifreeze coolant, suitable for stacks larger than 5 kW [39,40]	<ul style="list-style-type: none"> – Large cooling capability – Efficient cooling – Potential integration for fuel cell water management
Phase change material (PCM)	Evaporative [43] or boiling [44] cooling utilizing latent heat absorption during phase change	<ul style="list-style-type: none"> – Simplified system – Elimination of coolant pump

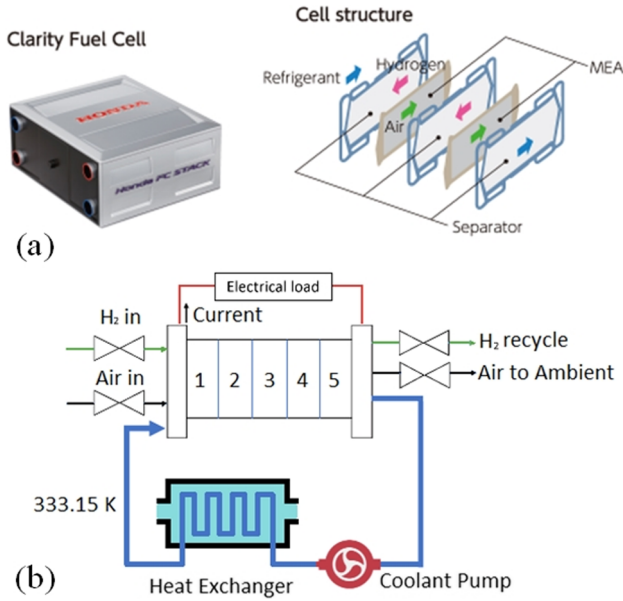


Fig. 1. (a) Cooling design in the Honda Clarity Fuel Cell stack [49]; (b) New cooling strategy: one cooling unit every five cells in this study [12].

inlet and outlet manifolds [24]. Manifolds may subject to flooding due to flow field expansion, affecting the uniformity of reactant gas supply among individual cells, which has been shown in the results of Minard et al. [25], Adroher and Wang [26] and Lewis and Wang [27].

Apart from experiment, three-dimensional (3D) multiphase non-isothermal modeling [28] is a popular and important method to reveal the complex transport phenomena in fuel cells. So far, a lot of 3D multiphase non-isothermal models have been developed, e.g. Zhang et al. [29], Wang and Wang [30], Perng and Wu [31], Wang and Chen [32] and Wu and Ku [33], etc. However, 3D simulation at the stack level is still limited due to computational burden [34]. Luo et al. [35] developed a 3D multiphase model to understand the cold start process in a fuel cell stack containing 3 single-channel cells. Macedo-Valencia et al. [36] conducted 3D single-phase simulation of a 5-cell stack without manifolds. Liu et al. [37] conducted 3D single-phase simulation of a 6-cell stack. The bipolar plate (BP) was simplified as two porous layers separated by a non-permeable plate. Le and Zhou [38] applied the 3D multi-phase model to a 3-cell stack including manifolds. The effect of liquid water on the stack performance was investigated.

Compared with internal combustion engine, PEM fuel cell stack cooling is more challenging due to the small temperature difference between stack

Table 3
Source terms.

Terms	Expressions
S_{H_2} ($\text{kg m}^{-3} \text{s}^{-1}$)	$-M_{H_2O} J_a / 2F$, ACL
S_{O_2} ($\text{kg m}^{-3} \text{s}^{-1}$)	$-M_{H_2O} J_c / 4F$, CCL
S_{H_2O} ($\text{kg m}^{-3} \text{s}^{-1}$)	$\begin{cases} -S_{v-1} & \text{GDL, MPL} \\ -S_{v-1} + S_{d-v} & \text{ACL} \\ -S_{v-1} + S_{d-v} + M_{H_2O} J_c / 2F & \text{CCL} \end{cases}$
S_g ($\text{kg m}^{-3} \text{s}^{-1}$)	$\begin{cases} -S_{v-1} + S_{d-v} - J_a M_{H_2} / 2F & \text{ACL} \\ -S_{v-1} + S_{d-v} - J_c M_{O_2} / 4F & \text{CCL} \\ -S_{v-1} & \text{GDLs and MPLs} \end{cases}$
S_{v-1} ($\text{kg m}^{-3} \text{s}^{-1}$)	$\begin{cases} \gamma_{v-1} \varepsilon (1-s) (C_{H_2O} - C_{sat}) M_{H_2O} & C_{H_2O} > C_{sat} \\ \gamma_{v-1} \varepsilon s (C_{H_2O} - C_{sat}) M_{H_2O} & C_{H_2O} < C_{sat} \end{cases}$
S_e (A m^{-3})	$\begin{cases} -J_a & \text{ACL} \\ J_c & \text{CCL} \end{cases}$
S_{ion} (A m^{-3})	$\begin{cases} J_a & \text{ACL} \\ -J_c & \text{CCL} \end{cases}$
S_{mw} ($\text{mol m}^{-3} \text{s}^{-1}$)	$\begin{cases} -S_{d-v} / M_{H_2O} - S_p & \text{ACL} \\ -S_{d-v} / M_{H_2O} + S_p & \text{CCL} \end{cases}$
S_{d-v} ($\text{kg m}^{-3} \text{s}^{-1}$)	$\gamma_{d-v} \rho_{mem} / EW (\lambda - \lambda_{eq}) M_{H_2O}$
S_p ($\text{mol m}^{-3} \text{s}^{-1}$)	$\frac{\rho_l k_{mem} (P_{ia} - P_{ic})}{\mu_l M_{H_2O} \delta_{mem} \delta_{CL}}$
S_T (W m^{-3})	$\begin{cases} \ \nabla \varphi_e\ ^2 \kappa_e^{eff} & \text{ABP} \\ \ \nabla \varphi_e\ ^2 \kappa_e^{eff} + S_{v-1} h & \text{GDLs, MPLs} \\ J_a \gamma_{act}^a ^2 + \ \nabla \varphi_e\ ^2 \kappa_e^{eff} + \ \nabla \varphi_{ion}\ ^2 \kappa_{ion}^{eff} & \text{ACL} \\ \quad + J_a \frac{\Delta S_a T}{2F} + (S_{v-1} - S_{d-v}) h & \\ J_c \gamma_{act}^c ^2 + \ \nabla \varphi_e\ ^2 \kappa_e^{eff} + \ \nabla \varphi_{ion}\ ^2 \kappa_{ion}^{eff} & \text{CCL} \\ \quad + J_c \frac{\Delta S_c T}{4F} + (S_{v-1} - S_{d-v}) h & \\ \ \nabla \varphi_{ion}\ ^2 \kappa_{ion}^{eff} & \text{Membrane} \\ S_{v-1} h & \text{Flow fields} \end{cases}$

and the ambient. Nevertheless, a very small amount of the heat produced in PEM fuel cell stacks can be removed by the reactant gases [39]. Consequently, increasing air stoichiometric ratio to cool down is usually suitable for stacks below 100 W [40]. For the stacks in the range of 200 W–2 kW, separate air cooling channel is necessary, and it needs to be replaced by liquid coolant (e.g. water) for stacks larger than 5 kW [39,40]. Apart from that, heat spreaders using thermally conductive graphite sheet [41] or heat pipe [42] or PCM (phase change material), e.g. evaporation [43] or boiling [44] have also been used in PEM fuel cell cooling. Table 1 listed the details of each cooling method mentioned above.

In FCVs, the PEM fuel cell stacks are usually in the range of tens to hundreds kilowatts and therefore liquid cooling is usually adopted. In order to improve cooling for each fuel cell, both Toyota Mirai [47] and

Table 2
Conservation equations.

Discriptions	Equations
Mass (gas)	$\frac{\partial}{\partial t} (\varepsilon (1-s) \rho_g) + \nabla \cdot (\rho_g u_g) = S_m$
Momentum (gas)	$\frac{\partial}{\partial t} \left(\frac{\rho_g u_g}{\varepsilon (1-s)} \right) + \nabla \cdot \left(\frac{\rho_g u_g u_g}{\varepsilon^2 (1-s)^2} \right) = -\nabla P_g - \frac{2}{3} \mu_g \nabla \cdot \left(\nabla \cdot \left(\frac{u_g}{\varepsilon (1-s)} \right) \right) + \mu_g \nabla \cdot \left(\nabla \cdot \left(\frac{u_g}{\varepsilon (1-s)} \right) + \nabla \cdot \left(\frac{u_g^T}{\varepsilon (1-s)} \right) \right) + S_u$
Species (gas)	$\frac{\partial}{\partial t} (\varepsilon (1-s) \rho_g Y_i) + \nabla \cdot (\rho_g u_g Y_i) = \nabla \cdot (\rho_g D_1^{eff} \nabla Y_i) + S_i$
Liquid pressure	$\frac{\partial}{\partial t} (\rho_l \varepsilon s) = \nabla \cdot \left(\rho_l \frac{kk_l}{\mu_l} \nabla P_l \right) + S_l$
Membrane water	$\frac{\rho_{mem}}{EW} \frac{\partial}{\partial t} (\omega \lambda) + \nabla \cdot \left(n_d \frac{j_{ion}}{F} \right) = \frac{\rho_{mem}}{EW} \nabla \cdot (D_d^{eff} \nabla \lambda) + S_{mw}$
Electric potential	$0 = \nabla \cdot (\kappa_e^{eff} \nabla \varphi_e) + S_e$
Ionic potential	$0 = \nabla \cdot (\kappa_{ion}^{eff} \nabla \varphi_{ion}) + S_{ion}$
Energy	$\frac{\partial}{\partial t} (\varepsilon \rho_1 C_{p,1} T + \varepsilon (1-s) \rho_g C_{p,g} T) + \nabla \cdot (\varepsilon \rho_1 C_{p,1} u_1 T + \varepsilon (1-s) \rho_g C_{p,g} u_g T) = \nabla \cdot (k^{eff} \nabla T) + S_T$

Table 4
Geometry parameters and operation conditions.

Parameter	Value
Manifold height (mm)	2.0
Manifold width (mm)	13.0
BP height (mm)	1.2
Channel height (mm)	1.0
Channel width (mm)	1.0
Rib width (mm)	1.0
Channel number	21
MEA area (cm ²)	50.4
MEA width (mm)	42.0
MEA length (mm)	120.0
GDL thickness (μm)	100.0
MPL thickness (μm)	20.0
CL thickness (μm)	10.0
Membrane thickness (μm)	25.4
Operation pressure (atm)	Anode: 2.5; Cathode: 2.5
Temperature (K)	333.15
Relative humidity	Anode: 1.0; Cathode: 1.0
Current density (A cm ⁻²)	1.0
stoichiometric ratio	Anode: 1.5; Cathode: 2.0

Hyundai NEXO [48] design 1 cooling unit for each cell. As the FCV maximum power demand is almost fixed, an apparent approach is to increase fuel cell performance, which has been the ultimate goal in many previous studies [17], for the stack volume reduction. In addition, decreasing the dimensions of some parts (e.g. bipolar plates and cooling units) is another major approach. A very recent review listed the typical dimension range for fuel cell component (see Table 4 in Ref. [12]). At the stack level, the simplifying of fastener is also important in reducing the volume of PEM fuel cell stack. For instance, the new fuel cell stack of Mirai uses 1-row (370 cells) to replace 2-rows (200 cells in each row) in 2008 model stack to reduce the endplate area [2], and get rid of spring using constant dimension tightening, instead of constant load fastening in 2008 model stack. In fact, by using 3D fine mesh flow field, high-performance MEA (membrane electrode assembly) and fastener optimization, its stack power density increased from 1.4 kW/L (0.83 kW/kg) in 2008 to 3.1 kW/L (2.0 kW/kg) [2]. Another approach, which has been examined for practical fuel cell, is to combine coolant and oxidant flow system [55]. However, this method cannot apply to high power stack due to the low heat capacity of air.

Table 5
Model parameters.

Parameter	Value
Porosity (GDL, MPL)	0.6, 0.6
Transfer coefficient	Anode: 0.5; Cathode: 0.5
Reference concentration (mol m ⁻³)	Hydrogen: 56.4; Oxygen: 3.39
Electric conductivity (MPL, CL, BP)	5000, 5000, 20,000
Membrane equivalent weight (kg mol ⁻¹)	1.1
Dry membrane density (kg m ⁻³)	1980
Contact angle (GDL, MPL, CL) (°)	110, 120, 95
Permeability (GDL, MPL, CL, membrane) (m ²)	2.0e-12, 1.0e-12, 1.0e-13, 2.0e-20
Condensation/evaporation rate (s ⁻¹)	100
Membrane water absorption or release rate (s ⁻¹)	1.3
Henry's constant (Pa m ⁻³ mol ⁻¹)	Hydrogen: 4560; Oxygen: 28,000
Pt loading (mg cm ⁻²)	Anode: 0.4; Cathode: 0.4
Exchange current density (A m ⁻²)	Anode: 10; Cathode: 1.5e-5
Pt/C ratio	0.35
Agglomerate radius (μm)	1.0
Electrolyte film thickness (nm)	80
Electrolyte fraction in agglomerate	0.226
Effective Pt surface ratio	0.5
GDL thermal conductivity (W m ⁻¹ K ⁻¹)	21, in-plane; 1.7, through-plane
Thermal conductivity (MPL, CL, membrane, BP) (W m ⁻¹ K ⁻¹)	1.0, 1.0, 0.95, 20
Heat specific capacity (GDL, MPL, CL, membrane, BP) (J kg ⁻¹ K ⁻¹)	568, 3300, 3300, 833, 1580

In general, increasing the number of cells per cooling unit is helpful in reducing stack volume but not favorable in local cooling. Honda Clarity introduces a cooling strategy of 1 cooling unit every two cells (Fig. 1 (a)) [49], which significantly reduce the volume of stack cooling unit. In this study, we extend the strategy to 5 cells per cooling unit (as a case study), which will yield further volume reduction. This case will clearly show the increased local temperature and reduced stack performance (For 2–3 cells per cooling unit, the reduced performance is not evident). This study shows that the new cooling strategy needs to be carefully designed for practical use in order to fully utilize its potential of volume reduction. A 3D multiphase non-isothermal model was employed to investigate this novel cooling strategy and temperature distribution, along with their

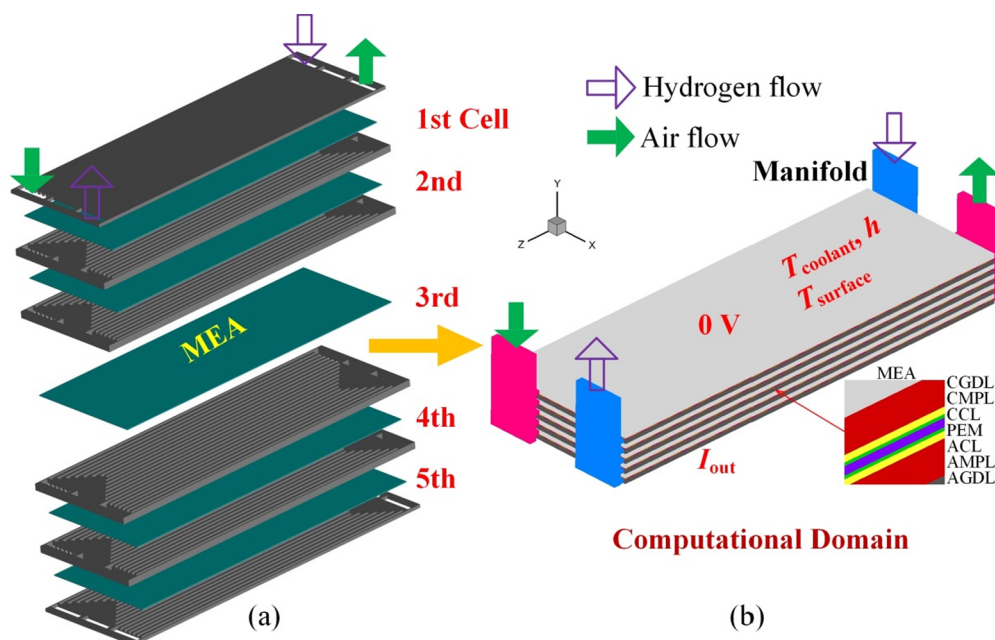


Fig. 2. Schematic and computational domain of the PEM fuel cell stack.

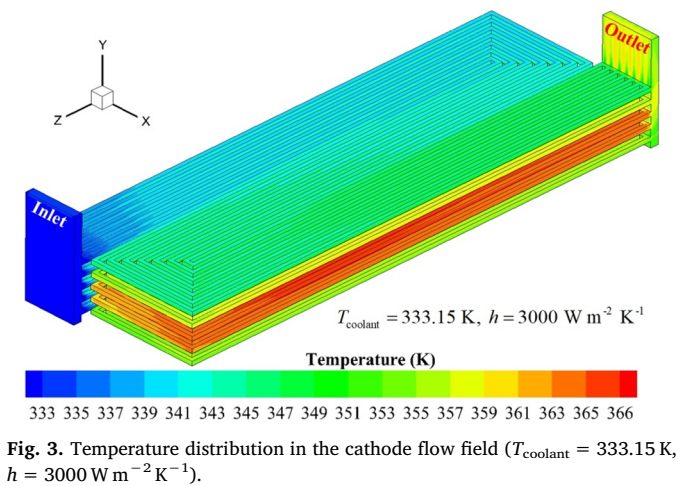


Fig. 3. Temperature distribution in the cathode flow field ($T_{\text{coolant}} = 333.15 \text{ K}$, $h = 3000 \text{ W m}^{-2} \text{ K}^{-1}$).

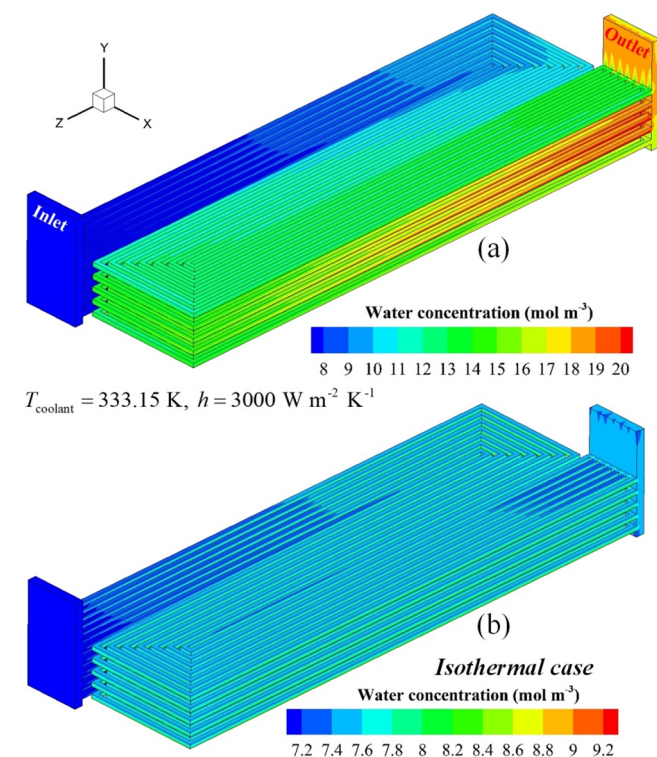


Fig. 4. Water vapor concentration distributions in the cathode flow fields.

impacts. For each cell, the MEA area is 50.4 cm^2 and 7-path serpentine flow fields were used for both anode and cathode. The inlet and outlet manifolds are included in the simulation. Two cooling conditions were investigated, including convective heat removal and constant temperature at the surfaces of the two endplates. Isothermal condition was also presented for comparison. The 3D multi-phase non-isothermal simulation in this study is of great significance to understanding of the complex heat and mass transport phenomena in a stack. The differences of water and thermal management at the stack and single fuel cell levels are also investigated in detail.

2. 3D multiphase non-isothermal model

2.1. Conservation equations

In this study, a 3D multiphase non-isothermal model was used to investigate the transport phenomena and electrochemical reactions in a PEM fuel cell stack. Table 2 lists the conservation equations with the

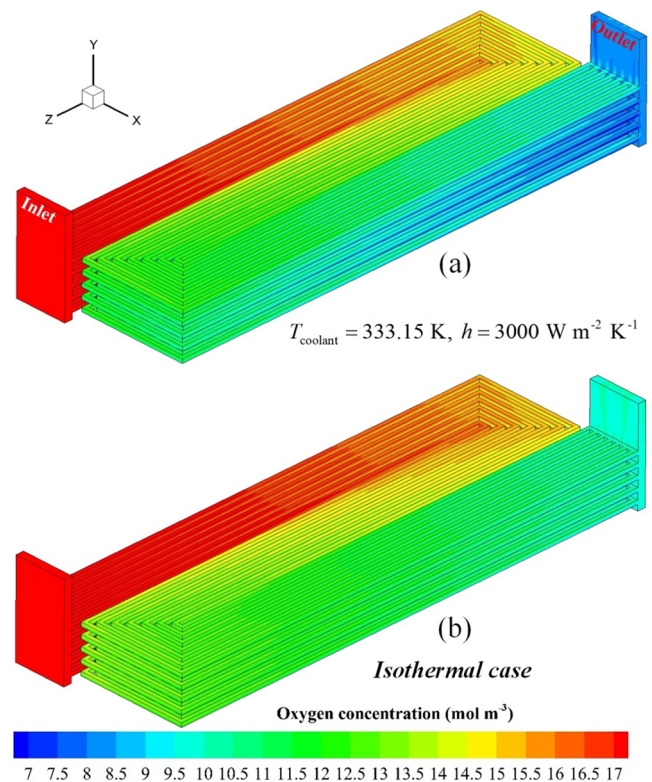


Fig. 5. Oxygen concentration distributions in the cathode flow fields.

corresponding source terms shown in Table 3. The continuity and Navier-Stokes equations describe the gas flows, which are assumed to be laminar because of low Reynolds numbers. The gas species conservation equations are used for hydrogen, oxygen, water vapor, and nitrogen. An individual liquid pressure conservation is added to describe the liquid water transport in gas diffusion layers (GDLs), micro-porous layers (MPLs) and catalyst layers (CLs), which are assumed to be homogenous porous media. In GDLs, the anisotropic electric and heat conductivity in the in-plane and through-plane directions are taken into account. A membrane water conservation equation describes the water transport in the membrane and CLs. The electron and proton transport is described by the electric and ionic charge conservation equations. The energy conservation equation predicts the temperature distribution in the stack. The model has been validated with several experimental data for single fuel cell [50], including the polarization curve and Ohmic loss. The only differences between the validated cases and this study are the computational domain and operation conditions. Other model parameters are the same. Detail of the model can be found in our previous study [50].

2.2. Boundary conditions

The mass flow rates and pressures are specified at the inlets and outlets, respectively [51]. As to the electric potential, a reference voltage (0 V) is set at the endplate surface of the cathode in the PEM fuel cell stack, as shown in Fig. 2(b). At the endplate surface of the anode, a constant output current density (I_{out}) is specified.

Cooling is important to the thermal management of fuel cell stacks where a number of cells are packed together with limited access for cooling. Table 1 compares a few cooling techniques for PEM fuel cells [12,39,40]. A simplest strategy is to add a separate cooling flow field for each of the cell [52], which however adds more costs to stack fabrication and is more prone to coolant leakage. Alternative is to add a cooling unit every a few fuel cells to reduce the number of required cooling units. In this study, we propose a cooling unit serves five cells, as shown in Fig. 1(b) and 2. The cooling conditions at the two sides of this stack are

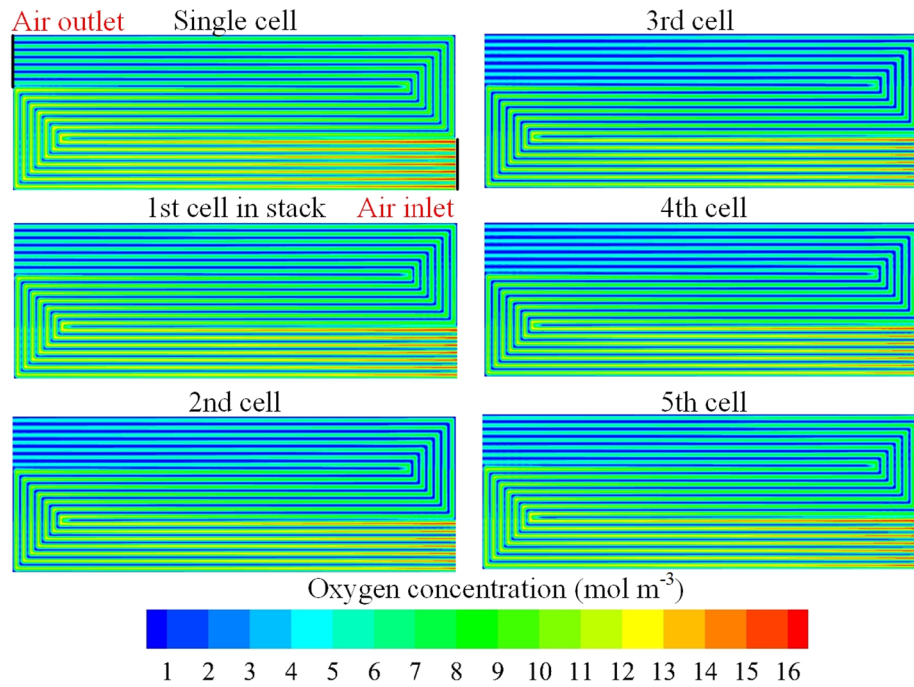


Fig. 6. Oxygen concentrations in the middle plane of the cathode CLs ($T_{\text{coolant}} = 333.15 \text{ K}$, $h = 3000 \text{ W m}^{-2} \text{ K}^{-1}$).

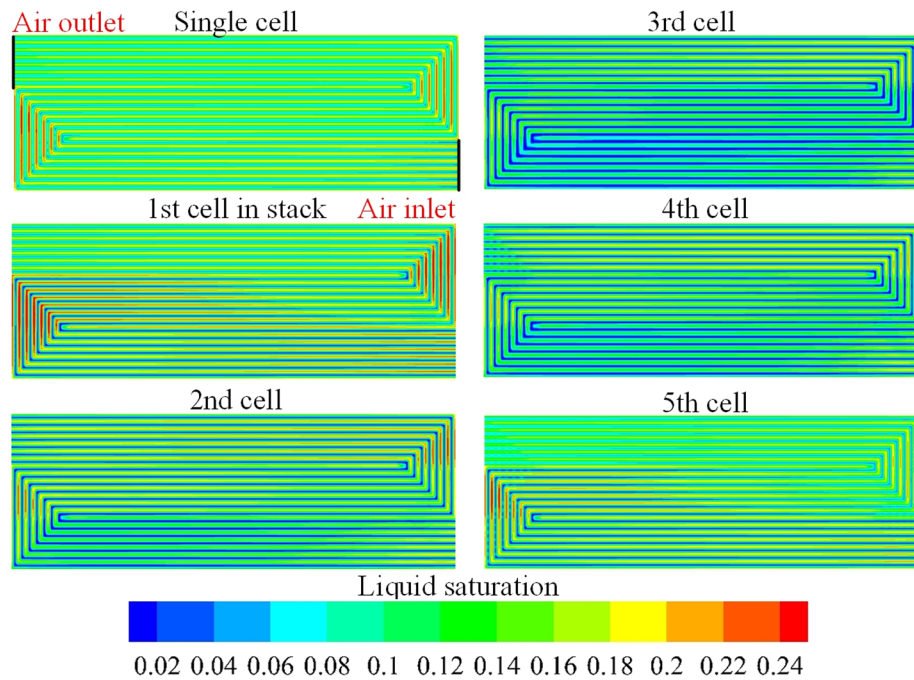


Fig. 7. Liquid saturation in the middle plane of the cathode CLs ($T_{\text{coolant}} = 333.15 \text{ K}$, $h = 3000 \text{ W m}^{-2} \text{ K}^{-1}$).

simplified as the convective thermal boundary conditions at the endplate surfaces. In practice, the optimal temperature of PEM fuel cell in FCVs usually ranges from 60 to 95 °C. Deionized water is a typical coolant, which is forced into stack by coolant pump. This corresponds to the forced convection heat transfer with a heat transfer coefficient usually ranging from 500 to 10,000 $\text{W m}^{-2} \text{ K}^{-1}$ [53]. We select the value of 3000 $\text{W m}^{-2} \text{ K}^{-1}$ for a case study. In general, this coefficient is dependent on a number of parameters such as the Pr and Re numbers, as given by typical correlations of the Nusselt number. While the coolant temperature corresponding to the lowest optimal operation temperature of PEM fuel cell (333.15 K) is selected in this study. Meanwhile, the coolant flow fields at two endplates of the stack are not considered in the computational

domain, as seen in Fig. 2. Their effects are simplified as convective heat transfer boundary conditions, in which the coolant temperature and corresponding convective heat transfer coefficient are set as 333.15 K and 3000 $\text{W m}^{-2} \text{ K}^{-1}$, respectively. Specifically, if the heat transfer coefficient is infinite large, the temperatures at the two endplate surfaces will equal to that of the coolant. As to other walls, the natural convection condition is specified, i.e. the room temperature of 298.15 K and heat transfer coefficient of 20 $\text{W m}^{-2} \text{ K}^{-1}$.

2.3. Numerical implementation

The schematic and computational domain of the short PEM fuel cell

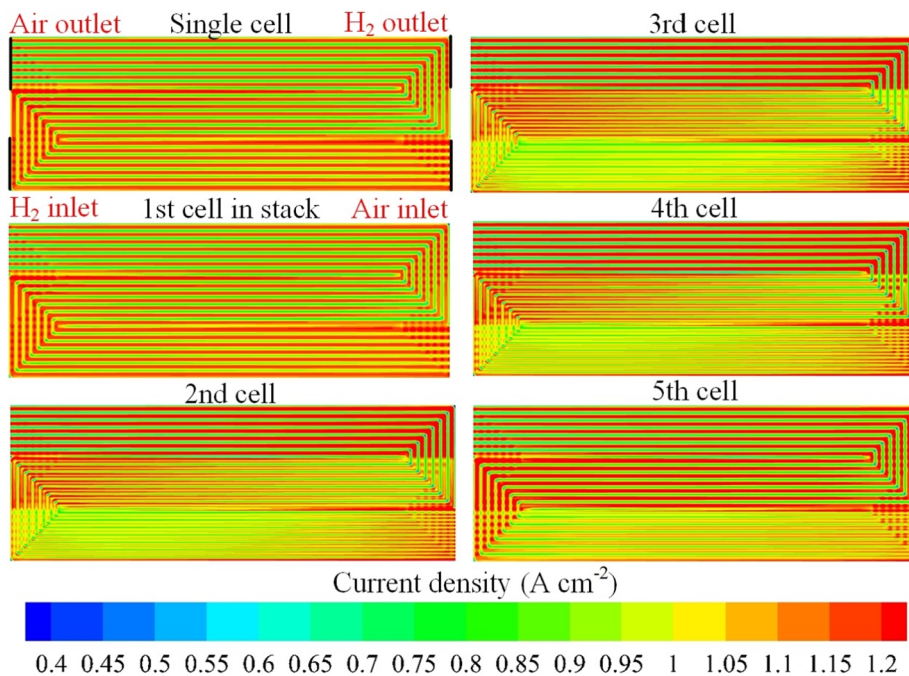


Fig. 8. Current density concentration in the middle plane of the membranes ($T_{coolant} = 333.15\text{ K}$, $h = 3000\text{ W m}^{-2}\text{ K}^{-1}$).

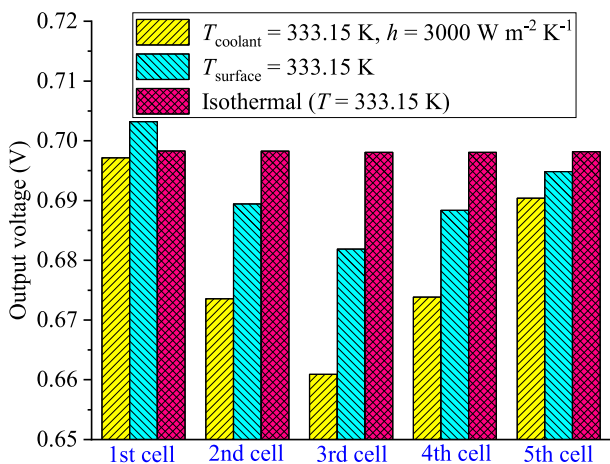


Fig. 9. Performance of each single cell in the stack under two thermal boundary conditions in comparison with isothermal operation.

stack in this study is shown in Fig. 2. There are 5 cells in the stack with each cell having a MEA area of 50.4 cm^2 and a length/width of $120.0/42.0\text{ mm}$. Both anode and cathode flow fields are 7-path serpentine with two U-turns, as shown in Fig. 2(a). The channel cross section size is $1.0\text{ mm} \times 1.0\text{ mm}$. Other geometry parameters and operation conditions and model parameters are listed in Tables 4 and 5. The hydrogen and air flows are arranged in the counter flow configuration. Total 3.14 million of computational cells are employed for this computational study. Each case took about 24 h using 8 processors on a small workstation (24 processors, Intel (R) Xeon (R) CPU E5-2620 v3 @ 2.40 GHz and 32 GB DDR RAM).

3. Results and discussion

3.1. Effect of temperature

In this study, the operation current density is kept as 1.0 A cm^{-2} for all simulation cases. Fig. 3 shows the temperature distribution in the cathode flow field at the convective thermal boundary conditions

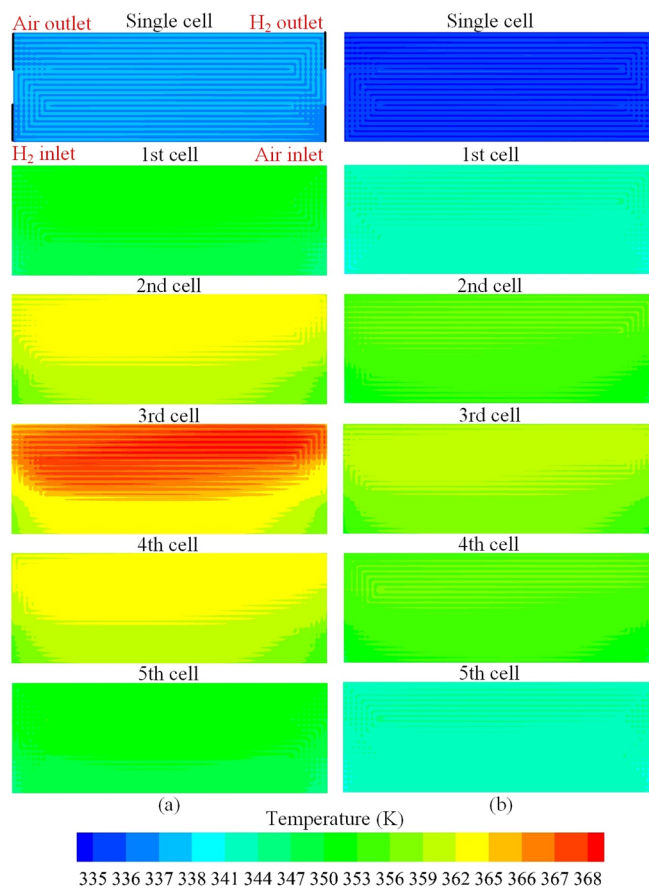


Fig. 10. Temperature distributions in the middle plane of the cathode CLs at the two thermal boundary conditions, (a): $T_{coolant} = 333.15\text{ K}$, $h = 3000\text{ W m}^{-2}\text{ K}^{-1}$; (b): $T_{surface} = 333.15\text{ K}$.

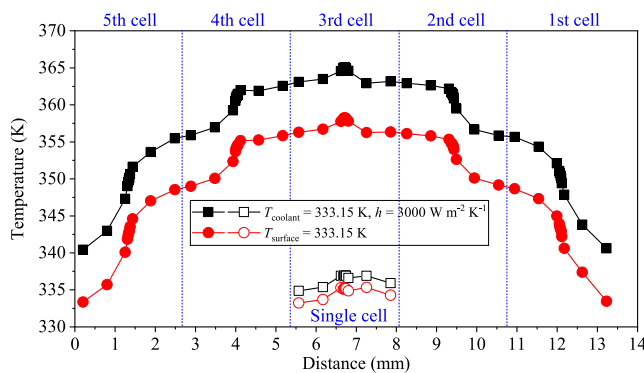


Fig. 11. Temperature profiles for the five cells in the stack.

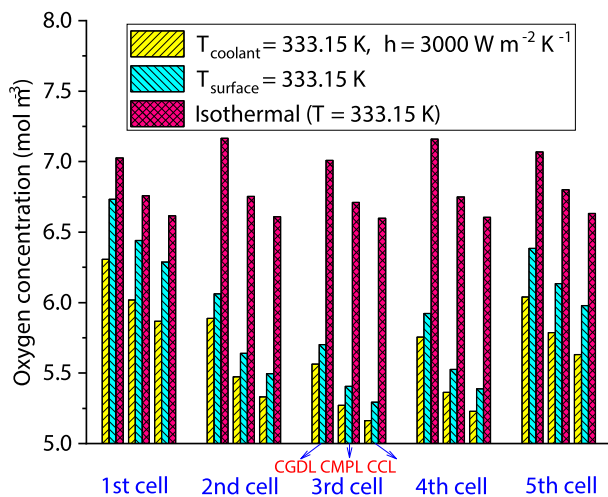


Fig. 12. Oxygen concentration of each single cell in the stack at the two thermal boundary conditions in comparison with the isothermal operation.

($T_{\text{coolant}} = 333.15 \text{ K}$, $h = 3000 \text{ W m}^{-2} \text{ K}^{-1}$). It is seen that the maximum temperature difference of higher than 30 K is present with the 3rd cell showing the maximum temperature. Comparing with the isothermal case (333.15 K), the much higher temperature in the non-isothermal case results in a much higher water vapor concentration due to the temperature dependence of the water saturation pressure, as shown in Fig. 4. Specially, the water concentrations in the 2nd, 3rd and 4th cells are much higher than those in the 1st and 5th cells. As a consequence, the oxygen concentration in the 3rd cell is the lowest due to the water vapor dilution, which can be seen in Fig. 5(a). As to the isothermal case, Fig. 5(b) shows that the oxygen concentrations in these 5 cells are almost the same. Thus, the temperature variation is the main cause to the non-uniform oxygen concentration distribution in the stack.

Fig. 6 shows the oxygen concentration distribution in the middle plane of the cathode CL. For comparison, a single-cell stack is also simulated at the same operation conditions and thermal boundary conditions. Overall, the oxygen concentration gradually decreases from the air inlet to outlet owing to the electrochemical reaction consumption. In addition, the oxygen concentration in the 3rd cell is the lowest, the 2nd and 4th cells are higher, and the 1st and 5th cells are the highest. This is consistent with the aforementioned conclusion drawn from Fig. 5. Additionally, the oxygen concentration in the stack is slightly lower than that in the single-cell case. This indicates that the reactant gas distribution in the stack may be worse than single-cell case because of higher temperature, which will be discussed in detail in the next section.

The liquid saturation distribution in the 5-cell stack is shown in Fig. 7, which shows that the liquid saturation in the 3rd cell is lowest because of the local high temperature. Fig. 8 shows the current density

distribution in the middle plane of the membrane, indicating large differences among the cells in the stack. The 3rd cell shows the most non-uniform current distribution. The current density in the upstream area is lower than that in the downstream area in this cell because of the low membrane water content caused by the high temperature [54].

3.2. Effect of thermal boundary condition

Fig. 9 shows the output voltages of each cell in this 5-cell stack for the two thermal boundary conditions, along with the isothermal case. For the isothermal case, the output voltages are almost the same among individual cells and mostly the highest except the 1st one for the three cases. There is a large variation in the output voltage among the cells in the stack for the non-isothermal cases. In addition, the variation in the case of the convective boundary condition is much larger than that of the constant surface temperature boundary condition. The latter corresponds to the lower temperature difference in the stack, as shown in Figs. 10 and 11. In general, the 3rd cell shows the worst performance, the 2nd and 4th cells are better and 1st and 5th cells are the best, as a result of the non-uniform oxygen concentration distribution as shown in Fig. 12, consistent with Fig. 5.

Fig. 10 shows the temperature distribution in the middle plane of the cathode CL. It is seen that the temperatures in all the cells of the stack are higher than that of the single-cell case. The temperature variation is also significant for the stack, especially for the 3rd cell. In the 2nd, 3rd and 4th cells, the peak temperature occurs in the downstream area because of the high current density in local (Fig. 8). In addition, Fig. 11 shows the temperature profiles for the five cells in the stack, whose shapes are consistent with that in previous studies, e.g. Hashmi [40], Wu et al. [55] and Pei et al. [56]. In particular, the maximum temperatures in the single cell and 5-cell stack are about 2 and 25 K, respectively, which are almost the same as that shown in Ref. [40]. It can be seen in Fig. 11 that the temperature difference at the same location between the two different thermal boundary conditions is about 6.9 K. In comparison, the difference in the single cell is only about 1.7 K between the two boundary conditions. This indicates that thermal management is much more important to a stack than a single cell.

In addition, the high temperature in the stack also cause low membrane hydration and water content, as shown in Fig. 13. This is a main cause to the low cell performance, especially for the 3rd cell in this stack. The low membrane water content in the upstream area also decreases local current density, increasing the non-uniform distribution, as shown in Fig. 8.

4. Conclusions

In this study, a three-dimensional (3D) multiphase non-isothermal model was employed to investigate a new cooling strategy for fuel cell stacks, i.e. one cooling unit every 5 fuel cells, which will significantly reduce the stack volume and weight. Two thermal boundary conditions were simulated and compared: one is the convective thermal boundary, and the other is the constant temperature boundary. It was found that the maximum temperature variation in this stack is as large as 30 K, which is a main cause to the observed non-uniform distributions of the oxygen concentration, liquid water, current density and membrane hydration among the 5 fuel cells. In general, the middle cell in the stack showed the lowest performance when the impact of non-isothermal condition is taken into account. For the isothermal case, the performances of individual cells were almost the same, so as the oxygen concentration distributions. In addition, it was found that the non-uniform oxygen concentration distribution in the stack resulted from the water vapor dilution due to the increased water saturation pressure at high temperature. The poor and non-uniform cell performances in this 5-cell stack were mainly caused by the non-uniform and diluted oxygen concentration distribution and low membrane hydration. It is

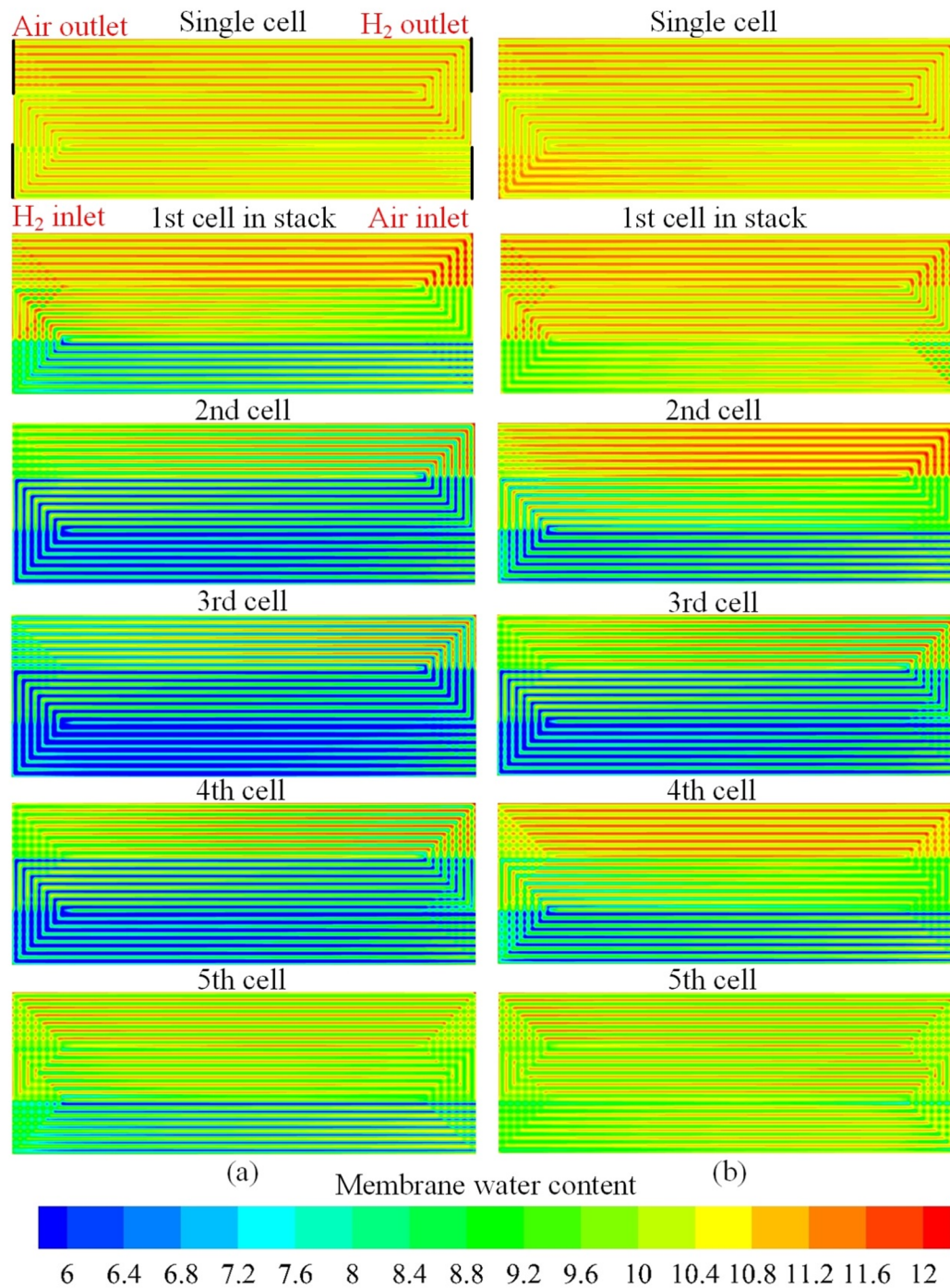


Fig. 13. Membrane water content in the middle plane of the membranes at the two thermal boundary conditions, (a): $T_{\text{coolant}} = 333.15 \text{ K}$, $h = 3000 \text{ W m}^{-2} \text{ K}^{-1}$; (b): $T_{\text{surface}} = 333.15 \text{ K}$.

important to carefully design the new cooling strategy for fuel cell stacks using 3D numerical simulation tools and a high heat transfer coefficient between the stack and coolant is desirable in this strategy to mitigate local overheating and cell performance reduction.

Acknowledgements

This work is supported by the National Key Research and Development Program of China (Grant No. 2017YFB0102703), and the China-UK International Cooperation and Exchange Project (Newton Advanced Fellowship) jointly supported by the National Natural Science Foundation of China (Grant No. 51861130359) and the UK

Royal Society (Grant No. NAF\R1\180146), and the National Natural Science Foundation of Tianjin (China) for Distinguished Young Scholars (Grant No. 18JCJQC46700). Y. Wang thanks Shanghai Everpower Technologies Ltd for partial financial support.

References

- [1] Wang Y, Chen KS, Mishler J, Cho SC, Adroher XC. A review of polymer electrolyte membrane fuel cells: technology, applications, and needs on fundamental research. *Appl Energy* 2011;88(4):981–1007.
- [2] Yoshida T, Kojima K. Toyota MIRAI fuel cell vehicle and progress toward a future hydrogen society. *Electrochem Soc Interface* 2015;24(2):45–9.
- [3] Matsunaga M, Fukushima T, Ojima K. Powertrain system of Honda FCX Clarity fuel

- cell vehicle. *World Electr Vehicle J* 2009;3(4):820–9.
- [4] Wilberforce T, Alaswad A, Palumbo A, Dassisti M, Olabi AG. Advances in stationary and portable fuel cell applications. *Int J Hydrogen Energy* 2016;41(37):16509–22.
- [5] Thounthong P, Raël S, Davat B. Control strategy of fuel cell and supercapacitors association for a distributed generation system. *IEEE Trans Ind Electron* 2007;54(6):3225–33.
- [6] Kumaraswamy VK, Quaicoe JE. Tracking techniques for the PEMFC in portable applications. 2016 IEEE Electrical Power and Energy Conference (EPEC). IEEE; 2016. p. 1–6.
- [7] Wang FC, Chen HC. The development and optimization of customized hybrid power systems. *Int J Hydrogen Energy* 2016;41(28):12261–72.
- [8] Keim M, Kallo J, Friedrich KA, Werner C, Saballus M, Gores F. Multifunctional fuel cell system in an aircraft environment: An investigation focusing on fuel tank inerting and water generation. *Aerosp Sci Technol* 2013;29(1):330–8.
- [9] <https://www.motortrend.com/cars/toyota/mirai/2017/> [accessed on August 11, 2019].
- [10] <https://www.wardsauto.com/10-best-engines/2018-wards-10-best-engines-mainstream-brands-triumph> [accessed on August 11, 2019].
- [11] <https://www.wardsauto.com/2019-10-best-engines/2019-wards-10-best-engines-gasoline-diesel-electrification-honored> [accessed on August 11, 2019].
- [12] Wang Y, Diaz DFR, Chen KS, Wang Z, Adroher XC. Materials, technological status, and fundamentals of PEM fuel cells—a review. *Mater Today* 2019. <https://doi.org/10.1016/j.matod.2019.06.005>. [in press].
- [13] Niu Z, Bao Z, Wu J, Wang Y, Jiao K. Two-phase flow in the mixed-wettability gas diffusion layer of proton exchange membrane fuel cells. *Appl Energy* 2018;232:443–50.
- [14] Wang Y, Chen KS, Cho SC. PEM fuel cells: thermal and water management fundamentals. Momentum Press; 2013.
- [15] Jiao K, Li X. Water transport in polymer electrolyte membrane fuel cells. *Prog Energy Combust Sci* 2011;37(3):221–91.
- [16] Zhang G, Xie X, Xie B, Du Q, Jiao K. Large-scale multi-phase simulation of proton exchange membrane fuel cell. *Int J Heat Mass Transf* 2019;130:555–63.
- [17] Konno N, Mizuno S, Nakaji H, Ishikawa Y. Development of compact and high-performance fuel cell stack. *SAE Int J Alternat Powertr* 2015;4(1):123–9.
- [18] Miller M, Bazylak A. A review of polymer electrolyte membrane fuel cell stack testing. *J Power Sour* 2011;196(2):601–13.
- [19] Devrim Y, Devrim H, Eroglu I. Development of 500 W PEM fuel cell stack for portable power generators. *Int J Hydrogen Energy* 2015;40(24):7707–19.
- [20] Amirfazli A, Asghari S, Sarraf M. An investigation into the effect of manifold geometry on uniformity of temperature distribution in a PEMFC stack. *Energy* 2018;145:141–51.
- [21] Wen CY, Lin YS, Lu CH. Experimental study of clamping effects on the performances of a single proton exchange membrane fuel cell and a 10-cell stack. *J Power Sour* 2009;192(2):475–85.
- [22] Weng FB, Jou BS, Su A, Chan SH, Chi PH. Design, fabrication and performance analysis of a 200 W PEM fuel cell short stack. *J Power Sour* 2007;171(1):179–85.
- [23] Chen CH, Jung SP, Yen SC. Flow distribution in the manifold of PEM fuel cell stack. *J Power Sour* 2007;173(1):249–63.
- [24] Wang Y, Basu S, Wang CY. Modeling two-phase flow in PEM fuel cell channels. *J Power Sour* 2008;179(2):603–17.
- [25] Minard KR, Viswanathan VV, Majors PD, et al. Magnetic resonance imaging (MRI) of PEM dehydration and gas manifold flooding during continuous fuel cell operation. *J Power Sour* 2006;161(2):856–63.
- [26] Adroher XC, Wang Y. Ex situ and modeling study of two-phase flow in a single channel of polymer electrolyte membrane fuel cells. *J Power Sour* 2011;196(22):9544–51.
- [27] Lewis JM, Wang Y. Investigating the pressure loss associated with two-phase flow in a rectangular microchannel suddenly expanding into a manifold. *Int J Hydrogen Energy* 2018;43(36):17444–60.
- [28] Zhang G, Jiao K. Multi-phase models for water and thermal management of proton exchange membrane fuel cell: a review. *J Power Sour* 2018;391:120–33.
- [29] Zhang G, Fan L, Sun J, Jiao K. A 3D model of PEMFC considering detailed multi-phase flow and anisotropic transport properties. *Int J Heat Mass Transf* 2017;115:714–24.
- [30] Wang Y, Wang CY. A nonisothermal, two-phase model for polymer electrolyte fuel cells. *J Electrochem Soc* 2006;153(6):A1193–200.
- [31] Peng SW, Wu HW. A three-dimensional numerical investigation of trapezoid baffles effect on non-isothermal reactant transport and cell net power in a PEMFC. *Appl Energy* 2015;143:81–95.
- [32] Wang Y, Chen KS. Advanced control of liquid water region in diffusion media of polymer electrolyte fuel cells through a dimensionless number. *J Power Sour* 2016;315:224–35.
- [33] Wu HW, Ku HW. The optimal parameters estimation for rectangular cylinders installed transversely in the flow channel of PEMFC from a three-dimensional PEMFC model and the Taguchi method. *Appl Energy* 2011;88(12):4879–90.
- [34] Wang Y, Chen KS. Modeling of polymer electrolyte membrane fuel cells and stacks. *Fuel Cell Sci Eng Mater Process Syst Technol* 2012:879–916.
- [35] Luo Y, Guo Q, Du Q, Yin Y, Jiao K. Analysis of cold start processes in proton exchange membrane fuel cell stacks. *J Power Sour* 2013;224:99–114.
- [36] Macedo-Valencia J, Sierra JM, Figueroa-Ramírez SJ, Diaz SE, Meza M. 3D CFD modeling of a PEM fuel cell stack. *Int J Hydrogen Energy* 2016;41(48):23425–33.
- [37] Liu Z, Mao Z, Wang C, Zhuge W, Zhang Y. Numerical simulation of a mini PEMFC stack. *J Power Sour* 2006;160(2):1111–21.
- [38] Le AD, Zhou B. A numerical investigation on multi-phase transport phenomena in a proton exchange membrane fuel cell stack. *J Power Sour* 2010;195(16):5278–91.
- [39] Zhang G, Kandlikar SG. A critical review of cooling techniques in proton exchange membrane fuel cell stacks. *Int J Hydrogen Energy* 2012;37(3):2412–29.
- [40] Hashmi SMH. Cooling strategies for PEM FC stacks. Chapter 6: PEM fuel cell stack calculations; 2010.
- [41] Wen CY, Huang GW. Application of a thermally conductive pyrolytic graphite sheet to thermal management of a PEM fuel cell. *J Power Sour* 2008;178(1):132–40.
- [42] Faghri A, Guo Z. Integration of heat pipe into fuel cell technology. *Heat Transfer Eng* 2008;29(3):232–8.
- [43] Perry ML, Meyers JP, Darling RM, Evans C, Balliet R. Evaporatively-cooled pem fuel-cell stack and system. *ECS Trans* 2006;3(1):1207–14.
- [44] Garrity PT, Klausner JF, Mei R. A flow boiling microchannel evaporator plate for fuel cell thermal management. *Heat Transfer Eng* 2007;28(10):877–84.
- [45] Schmidt H, Buchner P, Datz A, Dennerlein K, Waidhas M. Low-cost air-cooled PEFC stacks. *J Power Sour* 2002;105(2):243–9.
- [46] Yu SH, Sohn S, Nam JH, Kim CJ. Numerical study to examine the performance of multi-pass serpentine flow-fields for cooling plates in polymer electrolyte membrane fuel cells. *J Power Sour* 2009;194(2):697–703.
- [47] <https://car.watch.impress.co.jp/docs/news/impression/676634.html> [accessed on August 11, 2019].
- [48] <http://www.elecfans.com/d/716080.html> [accessed on August 11, 2019].
- [49] <https://global.honda/innovation/FuelCell/Clarity-Fuel-Cell-picturebook.html> [accessed on June 10, 2019].
- [50] Zhang G, Xie B, Bao Z, Niu Z, Jiao K. Multi-phase simulation of proton exchange membrane fuel cell with 3D fine mesh flow field. *Int J Energy Res* 2018;42(15):4697–709.
- [51] Zhang G, Jiao K, Wang R. Three-dimensional simulation of water management for high-performance proton exchange membrane fuel cell. *SAE Int J Alternat Powertr* 2018;7(2018-01-1309):233–47.
- [52] Wang Y, Wang CY. Ultra large-scale simulation of polymer electrolyte fuel cells. *J Power Sour* 2006;153(1):130–5.
- [53] Incropera FP, Lavine AS, Bergman TL, DeWitt DP. Fundamentals of heat and mass transfer. Wiley; 2007.
- [54] Carnes B, Spornjak D, Luo G, Hao L, Chen KS, Wang CY, et al. Validation of a two-phase multidimensional polymer electrolyte membrane fuel cell computational model using current distribution measurements. *J Power Sour* 2013;236:126–37.
- [55] Wu J, Galli S, Lagana I, Pozio A, Monteleone G, Yuan XZ, et al. An air-cooled proton exchange membrane fuel cell with combined oxidant and coolant flow. *J Power Sour* 2009;188(1):199–204.
- [56] Pei H, Liu Z, Zhang H, Yu Y, Tu Z, Wan Z, et al. In situ measurement of temperature distribution in proton exchange membrane fuel cell I a hydrogen–air stack. *J Power Sour* 2013;227:72–9.